Materials Horizons

ROYAL SOCIETY OF CHEMISTRY

COMMUNICATION

View Article Online
View Journal | View Issue

Cite this: *Mater. Horiz.*, 2025, 12, 9069

Received 13th June 2025,
Accepted 26th August 2025

DOI: 10.1039/d5mh01127b

rsc.li/materials-horizons

Is high specific surface area essential for anode catalyst supports in proton exchange membrane water electrolysis?

Kejie Lao,†[ab] Xinru Liu,†[ab] Huihong Lin,[ab] Linrui Wen,[abc] Yaping Pan,[ab] Tian Hu,[ab] Hua Bing Tao *[ab] and Nanfeng Zheng [ab]

Dispersing iridium onto high-specific-surface-area supports is a widely adopted strategy to maximize iridium utilization in anode catalysts of proton exchange membrane water electrolysis (PEMWE). However, here we demonstrate that the overall cell performance, including initial efficiency and long-term stability, does not benefit from the typical high specific surface area of catalyst supports. The conventional understanding that high iridium utilization on high-specific-surface-area supports increases activity holds only in aqueous electrolytes, while under the typical working conditions of PEMWE, the mass transport within the anode catalyst layers plays a more significant role in the overall performance. Particularly, the iridium oxide on the supports with 10-fold lower specific surface area exhibited an almost 3-fold lower decay rate without sacrificing original performance, owing to the enhanced mass transport enabled by the porous electrode structure. By further decreasing the Ir loading of catalysts, the advantages of low-surface-area supports became more pronounced, as the resulting anode achieved both enhanced performance and durability—demonstrating a 98 mV lower cell voltage and maintaining an exceptionally low degradation rate of only 8.8 μV h^{-1} over 1900 hours at 2.0 A cm^{-2}, corresponding to a nearly 10-fold improvement. These findings can help guide the rational design of catalysts for practical, low-cost PEMWE.

New concepts

This work challenges the conventional belief in proton exchange membrane (PEM) water electrolysis that high-specific-surface-area catalyst supports are inherently advantageous, revealing instead that they can hinder mass transport at high current densities. By systematically comparing supports with different particle sizes, we demonstrate that large-particle, low-surface-area supports markedly enhance reactant and product transport, achieving a 2.5-fold increase in catalyst utilization and a 98 mV reduction in cell voltage at 2.0 A cm^{-2}. This breakthrough overturns the prevailing paradigm in electrocatalyst design, which prioritizes maximizing the surface area and highlights the importance of tailoring the electrode structure to mitigate transport limitations under demanding operational conditions. Furthermore, the optimized supports exhibit nearly tenfold lower degradation rates (8.8 μV h^{-1} over 1900 h), offering a practical pathway toward durable and cost-effective PEM electrolyzers. Beyond the immediate application, this concept provides new insight into the trade-offs between surface area, transport efficiency, and stability, opening new avenues for materials design in electrochemical energy conversion.

Introduction

Catalyst supports play a key role in optimizing both the performance and cost of catalysts, especially for noble metal-based catalysts.[1,2] According to the conventional understanding, the high specific surface area benefits catalyst activity by enabling the extensive dispersion of noble metal sites.[3–6] This increased active site exposure improves accessibility for reactants, further boosting catalytic performance.[7,8] Additionally, high-specific-surface-area supports promote the formation of edge, corner, and vertex sites, which are coordinatively unsaturated and exhibit superior catalyst properties—a widely recognized phenomenon in nanocatalysis.[9,10] However, in practical applications, the necessity for high-specific-surface-area supports warrants further scrutiny, as a trade-off exists between catalyst activity and emerging industrial challenges—issues often overlooked in traditional liquid-phase electrolyte models.[11] For instance, in real-world scenarios like proton exchange membrane water electrolysis (PEMWE), systems operate at current densities one to two orders of magnitude higher than those used in ideal model systems, significantly amplifying mass transport demands for each active site.[12–14] The high current density worsens challenges related to water and bubble management, as meso- or

[a] *New Cornerstone Science Laboratory, State Key Laboratory for Physical Chemistry of Solid Surfaces, Collaborative Innovation Center of Chemistry for Energy Materials, and College of Chemistry and Chemical Engineering, Xiamen University, Xiamen, 361005, China. E-mail: hbtao@xmu.edu.cn*
[b] *Innovation Laboratory for Sciences and Technologies of Energy Materials of Fujian Province (IKKEM), Xiamen, 361005, China*
[c] *Amoy Island Hydrogen (Xiamen) Technology Co., Ltd, Xiamen, 361103, China*
† All authors contributed equally to this work.

microporous structures associated with high specific surface area hinder the formation of efficient gas transport channels.[15–17] In fact, they may accelerate electrode degradation at high current densities.[18] Therefore, balancing the specific surface area of supports with the performance requirements under PEMWE operating conditions remains a key challenge in the design of efficient anode catalysts.

In this work, we evaluated the performance of iridium-based catalysts supported on carriers with varying specific surface areas and found that the conventional preference for high-specific-surface-area supports was not suitable for practical PEMWE applications. Instead, large-particle supports with lower specific surface areas significantly influenced the structure of both the catalyst and the anode catalyst layer (ACL), leading to substantial improvements in PEMWE performance and stability. Large-particle supports facilitated the formation of continuous IrO_2 distributions, thereby enhancing electrical conductivity. Additionally, large-particle supports enabled the construction of a porous electrode, facilitating efficient mass transport. These synergistic effects greatly enhanced the utilization of precious metals and improved durability, achieving a minimal decay rate of only 8.8 μV h^{-1} over 1900 hours at 2.0 A cm^{-2}. This study highlighted the critical role of the support specific surface area in influencing both the catalyst intrinsic activity and its practical performance under operating conditions, providing a promising pathway toward achieving more efficient electrolyzers.

Results and discussion

Influence of the specific surface area of catalyst supports

In this study, TiO_2 was selected as the catalyst support due to its outstanding stability and cost-effectiveness,[19] and it is widely recognized as a representative anode catalyst support in industrial PEM water electrolysis applications. To investigate the influence of particle size, three different sizes of TiO_2 particles—25 nm, 100 nm, and 300 nm—were employed as supports (Fig. S1). The specific surface areas of TiO_2 particles vary significantly with particle size, as illustrated in Fig. 1a. Smaller TiO_2 particles, such as the 25 nm variant, exhibited a specific surface area nearly ten times larger than that of the 300 nm counterpart. Subsequently, the traditional Adams fusion method was used to load IrO_2 onto the three TiO_2 supports,[20] maintaining an IrO_2/TiO_2 mass ratio of 50%. Among the synthesized catalysts, the 25 nm catalyst had the largest specific surface area, whereas the 300 nm catalyst had the smallest specific surface area (Fig. S2a). This result indicated that the specific surface area of the catalysts was predominantly dictated by the TiO_2 support. Overall, all three catalysts exhibited relatively large specific surface areas, confirming effective and abundant loading of IrO_2 particles on the TiO_2 surfaces.[21]

Subsequently, oxygen evolution reaction (OER) performance tests were conducted for the three catalysts (Fig. 1b). The 25 nm–50% catalyst showed the best kinetic performance, achieving a Tafel slope of 43.4 mV dec^{-1}, which indicated superior intrinsic activity compared to 100 nm–50% (49.7 mV dec^{-1}) and 300 nm–50% (54.3 mV dec^{-1}). At η = 300 mV, the 25 nm–50% catalyst exhibited a mass activity 1.5 times higher than that of the 300 nm–50% catalyst (Fig. S2c). The observed differences in intrinsic activity can be attributed to structural variations among the catalysts. Scanning electron microscopy (SEM) analysis revealed that TiO_2 particle size significantly influences the distribution of IrO_2 (Fig. S3). At a fixed IrO_2/TiO_2 mass ratio, the high-specific-surface-area supports facilitated uniform and moderate IrO_2 loading, which exposed more active sites,[22] as indicated by the larger electrochemical double-layer capacitance (Fig. 1c).

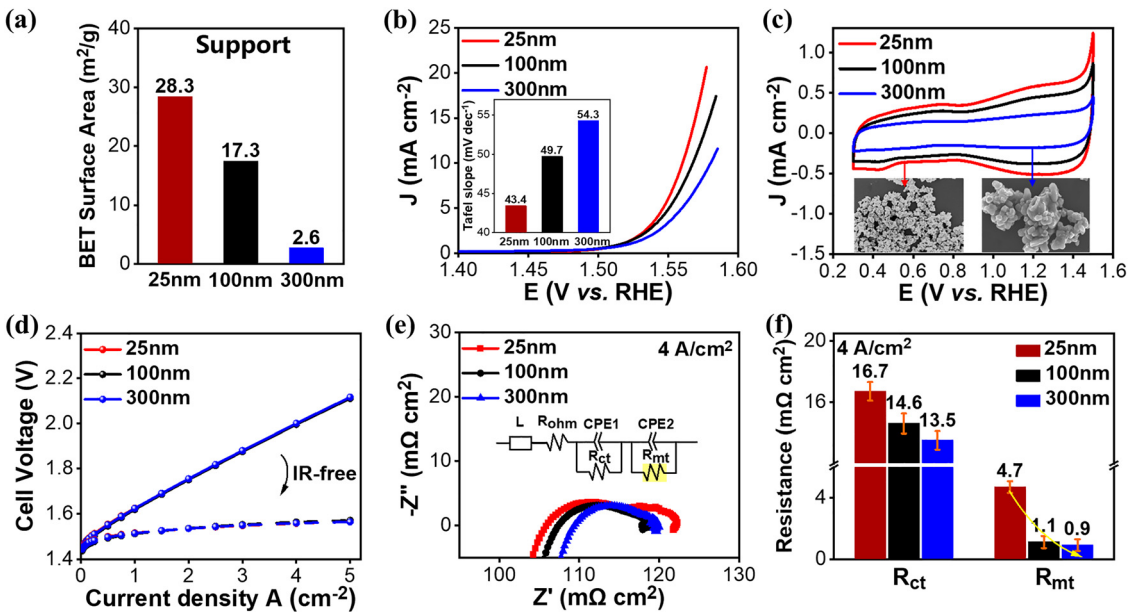

Fig. 1 Structures of catalysts with 50% loading and their performance in liquid electrolytes and devices. (a) Specific surface area of TiO_2 supports. (b) Linear sweep voltammetry curves in the RDE. (c) Cyclic voltammograms of three 50%-loaded catalysts, recorded at a scan rate of 50 mV s^{-1} in ideal liquid electrolytes. (d) Polarization curves in the PEMWE cell. (e) Nyquist plots of GEIS conducted at 4.0 A cm^{-2}. (f) Fitted R_{ct} and R_{mt} results of all ACLs.

Conversely, the low-specific-surface-area supports led to thick and uneven IrO_2 deposition, which obscured the original TiO_2 structure. Excessive IrO_2 accumulation caused partial coverage of active sites, making them inaccessible and reducing their availability.[23] These differences in support structure affected the utilization of noble metals, which directly influenced the intrinsic activity.[24]

As shown above, catalysts synthesized with supports of varying particle sizes displayed differences in intrinsic activity. However, when these catalysts were further fabricated into ACLs and tested in the PEMWE single-cell, no notable differences in performance were detected (Fig. 1d). In EIS tests, the 25 nm–50% ACL exhibited a more prominent low-frequency arc (Fig. 1e), associated with mass transport resistance (R_{mt}).[25] Fitting the Nyquist plots with an established equivalent circuit model (EEC) revealed that the R_{mt} of 25 nm–50% ACL was 4.7 mΩ cm^2, which is about five times greater than that of 300 nm–50% ACL (0.9 mΩ cm^2, Fig. 1f),[26] suggesting significant mass transport resistance. Additionally, with increasing current density, a reversal in charge transfer resistance (R_{ct}) was observed (Fig. S4). At 4 A cm^{-2}, the R_{ct} of 300 nm–50% was 3.2 mΩ cm^2 lower than that of 25 nm–50%, which contrasted with the activity trend observed in Fig. 1b. This suggests that hindered mass transport can suppress the expression of the catalyst intrinsic activity.[27] In summary, the absence of performance differences among catalysts with varying particle sizes in PEMWE may be attributed to the combined effects of catalyst intrinsic activity and ACL structure.

As previously noted, while catalysts with different particle sizes exhibited no significant performance differences in PEMWE, their stability varied markedly at 80 °C and 2 A cm^{-2}. The 300 nm–50% ACL exhibited superior stability, with a voltage degradation rate of 21.8 μV h^{-1} over 800 hours, compared to 61.0 μV h^{-1} for the 25 nm–50% ACL—three times higher (Fig. 2a). Polarization curves after the 800-hour stability test indicated that the primary difference was a substantial voltage increase at high current densities (Fig. 2b). Further voltage loss analysis revealed that stability differences among the three ACLs were primarily due to a significant increase in mass transport overpotential (Fig. 2c).

In long-term stability tests, Nyquist plots at 4 A cm^{-2} for the 25 nm–50% and 100 nm–50% ACLs showed distinct mass transport arcs and an increase in high-frequency resistance (HFR). In contrast, the 300 nm–50% ACL exhibited negligible mass transport arcs and lower HFR (Fig. 2d). EEC fitting results revealed that the R_{mt} of the 25 nm–50% ACL increased dramatically from 4.7 mΩ cm^2 to 65.6 mΩ cm^2 (Fig. 2e), representing a 13-fold rise and indicating severe mass transport hindrance. This phenomenon also impaired the expression of catalyst active sites, increasing R_{ct} by 31.7 mΩ cm^2 (a 189.8% rise).[28] In comparison, resistances in the 300 nm–50% ACL decreased slightly, likely due to the activation of the electrode during operation (Fig. 2e). Based on the previously discussed results of mass transport hindrance in small-particle-size supports, we proposed that the primary cause of the stability differences lies in the pore structure of the ACLs. The 300 nm–50% ACL may possess an abundant network of mesopores and macropores, facilitating more efficient water and gas transport.[29] In contrast, the limited pore space in the 25 nm–50% ACL limited the gas transport pathways and led to severe bubble accumulation, thereby generating additional overpotentials.[30,31]

Mechanistic study of catalyst supports on cell performance

To clarify the relationship between the ACL structure and performance, this study carried out detailed characterization

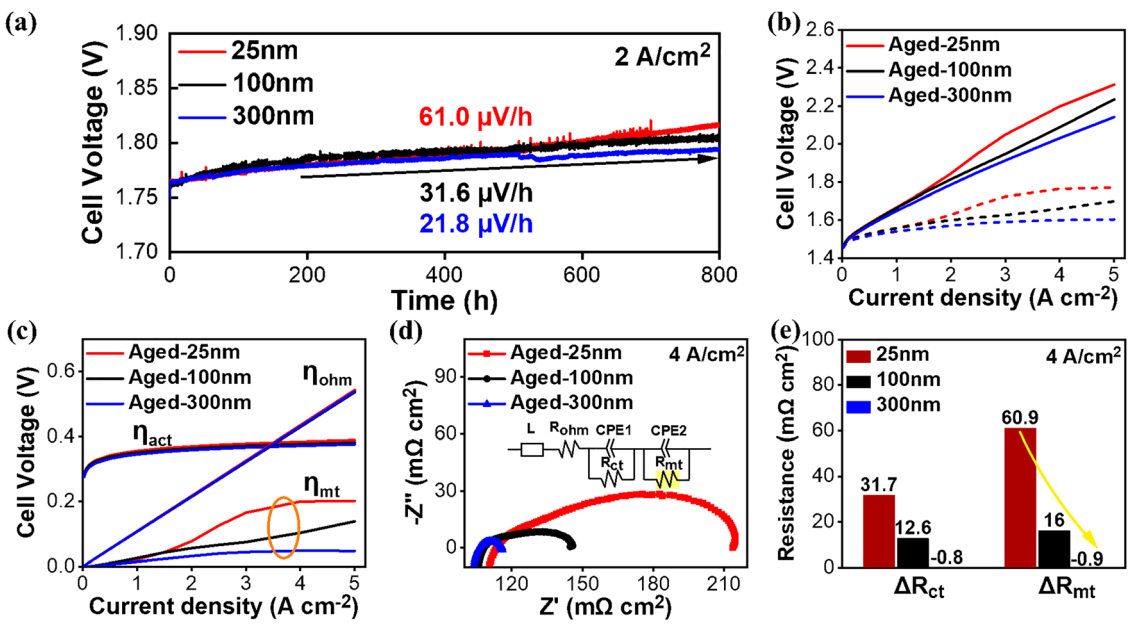

Fig. 2 Stability investigation of catalysts with 50% loading in a PEMWE cell. (a) Durability tests at 2.0 A cm^{-2} under 80 °C. (b) Polarization curves in the PEMWE cell over 800-hour durability at 80 °C and 2.0 A cm^{-2}. (c) Breakdown of cell voltage into various voltage losses of all aged-ACLs. (d) Nyquist plots of GEIS conducted at 4.0 A cm^{-2} after 800-hour durability. (e) Fitted R_{ct} and R_{mt} variation of all ACLs after 800-hour durability.

of ACLs prepared using the three catalysts. We first excluded the influence of ionomer spatial distribution within the ACL. As shown in Fig. S5a, cross-sectional SEM images of the ACLs revealed no evidence of ionomer agglomeration, and the catalyst particles exhibited well-defined boundaries without thick ionomer shells. Combined with further time-of-flight secondary ion mass spectrometry (ToF-SIMS) analysis (Fig. S5b and c), the results indicate that the ionomer is uniformly dispersed throughout the electrode, with no significant differences in ionomer distribution among the samples.

In contrast, under identical noble metal loadings, the noticeable differences in ACL thickness drew our attention, with the 300 nm–50% ACL displaying a more prominent porous structure in both cross-sectional and planar views (Fig. 3a and Fig. S5). Further pore characterization and size distribution analysis were conducted using nitrogen adsorption–desorption isotherms and mercury intrusion porosimetry (MIP). The results indicated that the 300 nm–50% ACL featured a more continuous pore distribution with a higher prevalence of mesopores and macropores (Fig. 3b and c). Specifically, the pore volume of the 300 nm–50% ACL was about 2.7 times greater than that of the 25 nm–50% ACL (0.43 $cm^3\ g^{-1}$ *vs.* 0.16 $cm^3\ g^{-1}$). MIP analysis showed that the 300 nm–50% ACL had a larger macropore size distribution (183 nm compared to 95 nm and 77 nm).

Differences in the pore structures of the ACLs provided a logical explanation for the performance variations of ACLs. The 300 nm–50% ACL exhibited higher porosity, providing more pathways for gas molecule flow.[32] Larger pores are generally linked to lower flow resistance, especially when pore connectivity is well-developed, enabling faster gas diffusion and reducing bubble accumulation.[33] In contrast, the 25 nm–50% ACL contained fewer and smaller pores, restricting gas diffusion space, slowing diffusion rates, and increasing the risk of the bubble shielding effect, which ultimately deactivated reactive sites (Fig. 3e).[16] To confirm the role of ACL porous structures in enabling efficient mass transport, cyclic voltammetry (CV) was employed to analyze oxygen accumulation behavior in different ACLs (Fig. S6).[34] The results indicated that the oxygen reduction current in the 300 nm–50% ACL was significantly lower than in the 25 nm–50% ACL, with accumulated charge being roughly half of that in the 25 nm–50% ACL (Fig. 3d). This suggested that oxygen diffusion in the 300 nm–50% ACL was faster, resulting in lower oxygen accumulation.

In summary, the porous structure of the 300 nm–50% ACL promoted efficient mass transport and optimal utilization of

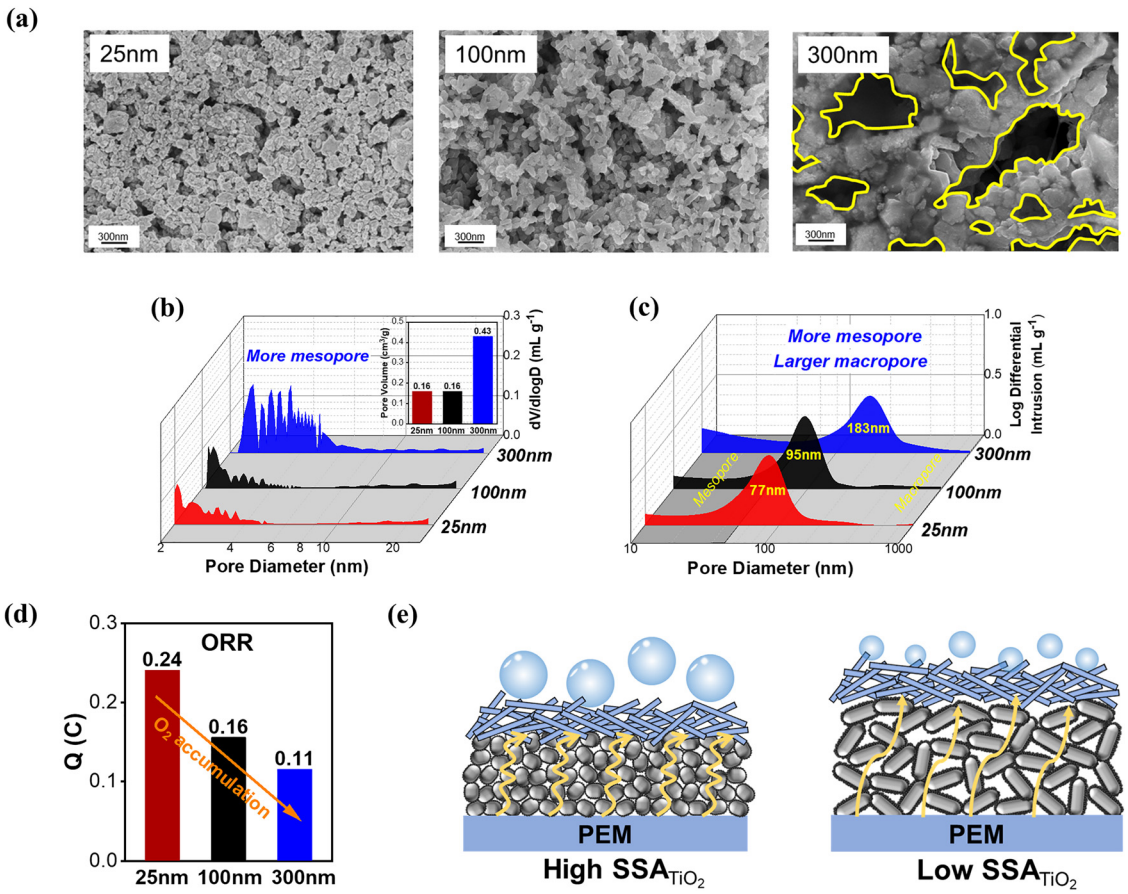

Fig. 3 Structural characterization and analysis of mass transport in the ACLs. (a) SEM images of all the ACLs with 50% loading catalysts. (b) and (c) Pore-size distribution curves. (d) The amount of charge accumulated by ORR current. (e) Schematic illustration of the high-SSA-TiO_2-based ACL and low-SSA-TiO_2-based ACL in PEMWE, respectively.

active sites. This structural advantage compensated for its lower intrinsic activity and markedly improved its long-term stability under operational conditions.

To gain deeper insight into the formation mechanism of ACL porous structures, the micro-dynamic process of catalyst ink was analyzed. Multiple light scattering techniques were employed to monitor changes in backscattered light intensity (ΔBS) over time for catalyst ink at 60 °C, offering insights into its dynamic behavior.[35,36] As shown in Fig. 4a and b, all catalyst inks exhibited ionomer floating and catalyst sedimentation dynamics. Notably, the sedimentation behavior of the 300 nm–50% ink was markedly more pronounced. During the first 5 hours, the ΔBS at the bottom rose rapidly by about 5% and then stabilized, indicating that the 300 nm catalysts rapidly assembled and reached equilibrium in the ink. This rapid sedimentation impeded further observation of ionomer floating. In contrast, the ΔBS of the 25 nm–50% ink exhibited continuous fluctuations, indicating ongoing ionomer floating and catalyst sedimentation. Even at the end of the test, the 25 nm–50% ink had not yet achieved a stable state.

After one week of resting, the 25 nm–50% ink still contained floating ionomers and smaller catalyst particles in the upper layer, whereas the 300 nm–50% ink exhibited a clarified upper layer and a sedimented lower layer composed of catalysts and ionomers. The sediment height of the 300 nm–50% catalyst was about 2.5 times greater than that of the 25 nm–50% catalyst (Fig. S7). As shown in Fig. 4d, this difference occurred because the 300 nm catalyst, with its greater steric hindrance, settled quickly, facilitating the formation of a more porous structure. In contrast, the 25 nm catalyst, characterized by smaller steric hindrance, sedimented more densely.[37] Although some smaller particles remained suspended in the upper layer, they tended to compact more tightly during subsequent sedimentation, impeding the formation of mesopores and macropores in the ACL.

Fig. 4c presents the viscosity curves and the corresponding values of various catalyst inks. The viscosity of the 300 nm–50% ink was markedly higher, approximately 5.5 times that of the 25 nm–50% ink (117.9 mPa s *vs.* 21.4 mPa s). The difference in ink viscosity is closely related to the catalyst packing volume.[38] As the catalyst volume fraction in the ink rises, particle interactions—such as compression and collision—intensify, leading to greater flow resistance and subsequently higher viscosity. Moreover, at higher shear rates, the 300 nm–50% ink exhibited a distinct shear-thinning behavior. This shear-thinning behavior suggests that the large-particle catalyst (300 nm), due to its greater spatial hindrance, encounters higher resistance to structural rearrangement, thereby exhibiting stronger shear resistance. This property further implies that the large-particle catalyst can better retain its structural stability under external shear forces, facilitating the formation of an ACL with a highly porous structure.

Design of more efficient catalysts with low-specific-surface area supports

To reduce noble metal content and improve utilization, this study reduced the IrO_2/TiO_2 mass ratio to 30% across all three catalysts. Under this reduced loading, the specific surface areas of the 25 nm and 100 nm catalysts decreased significantly, dropping to roughly half their values at 50% loading. In contrast, the 300 nm catalyst exhibited only a slight reduction in specific surface area (Fig. S8a). This observation suggested that the specific surface area was predominantly influenced by IrO_2 particles on the support surface. The 300 nm support accumulated more IrO_2 on its surface, but compared to the 50%

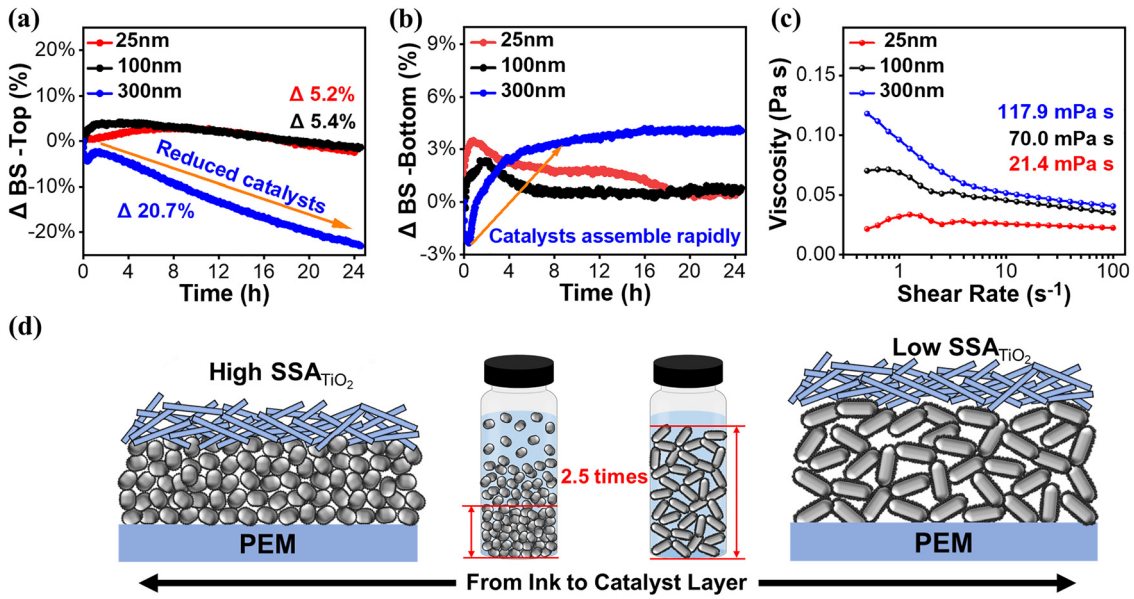

Fig. 4 Formation mechanism of ACL porous structures. (a) and (b) Variation in backscattering intensity (Delta BS) over 24 hours between the top and bottom layers of actual catalyst inks. (c) Steady-shear relative viscosity data of inks. (d) Illustration of the process from catalyst ink to catalyst layer formation.

loading, the IrO_2 content was more appropriate, and the support morphology remained well-defined (Fig. S9).

Scanning transmission electron microscopy (STEM) was employed to obtain high-angle annular dark-field (HAADF) images, alongside energy-dispersive X-ray spectroscopy (EDS) analysis of Ir (red) and Ti (blue) (Fig. 5a and c and Fig. S10). The results revealed that at identical IrO_2 loadings, larger-particle supports facilitated the formation of a more continuous noble metal shell, whereas smaller-particle supports exhibited a dispersed, discontinuous IrO_2 distribution. This structural variation directly impacted the electrical conductivity of the catalyst powder.[13] Conductivity measurements indicated that the electrical conductivity of 300 nm–30% was 9.3 S cm^{-1}—three times higher than that of 25 nm–50% (3.0 S cm^{-1}). The improved conductivity enhanced electron transfer between OER active sites, thereby influencing the intrinsic catalytic activity and, ultimately, overall performance. Further OER performance evaluations (Fig. 5b and Fig. S11) demonstrated that the 300 nm–30% catalyst exhibited the highest kinetic efficiency, with a Tafel slope of 40.0 mV dec^{-1} (Fig. S8b), outperforming the 100 nm–30% (40.8 mV dec^{-1}) and 25 nm–30% (46.9 mV dec^{-1}) catalysts. At η = 300 mV, its mass activity was 3.4 times greater than that of the 25 nm–30% catalyst (Fig. S8c). These findings underscore the crucial role of IrO_2 distribution continuity on the support surface in determining catalytic performance.[39]

After further preparation of these catalysts into ACLs, the 300 nm–30% ACL demonstrated outstanding performance in PEMWE. At 4 A cm^{-2}, its voltage was 1.979 V, 98 mV lower than the 25 nm–30% ACL, which operated at 2.077 V (Fig. 5d). Further analysis revealed that the performance differences primarily arose from variations in activation overpotential (η_{ct}), ohmic overpotential (η_{ohm}), and mass transport overpotential (η_{mt}) (Fig. S12a).[25] Specifically, differences in η_{ct} were consistent with RDE test results, where variations in conductivity influenced the charge transfer processes. Variations in catalyst conductivity also impacted the contact resistance between the ACL and the porous transport layer (PTL).[12] The HFR of the 300 nm–30% ACL was 104.9 mΩ cm^2, which was 7.7 mΩ cm^2 lower than that of the 25 nm–30% ACL. This difference in HFR was reflected in η_{ohm}. Additionally, variations in η_{mt} were mainly related to water and gas transport. The R_{mt} of the 25 nm–30% ACL was five times greater than that of the 300 nm–30% ACL (Fig. S12c and d), driven by differences in ACL pore structures. Further quantitative analysis at 4 A cm^{-2}

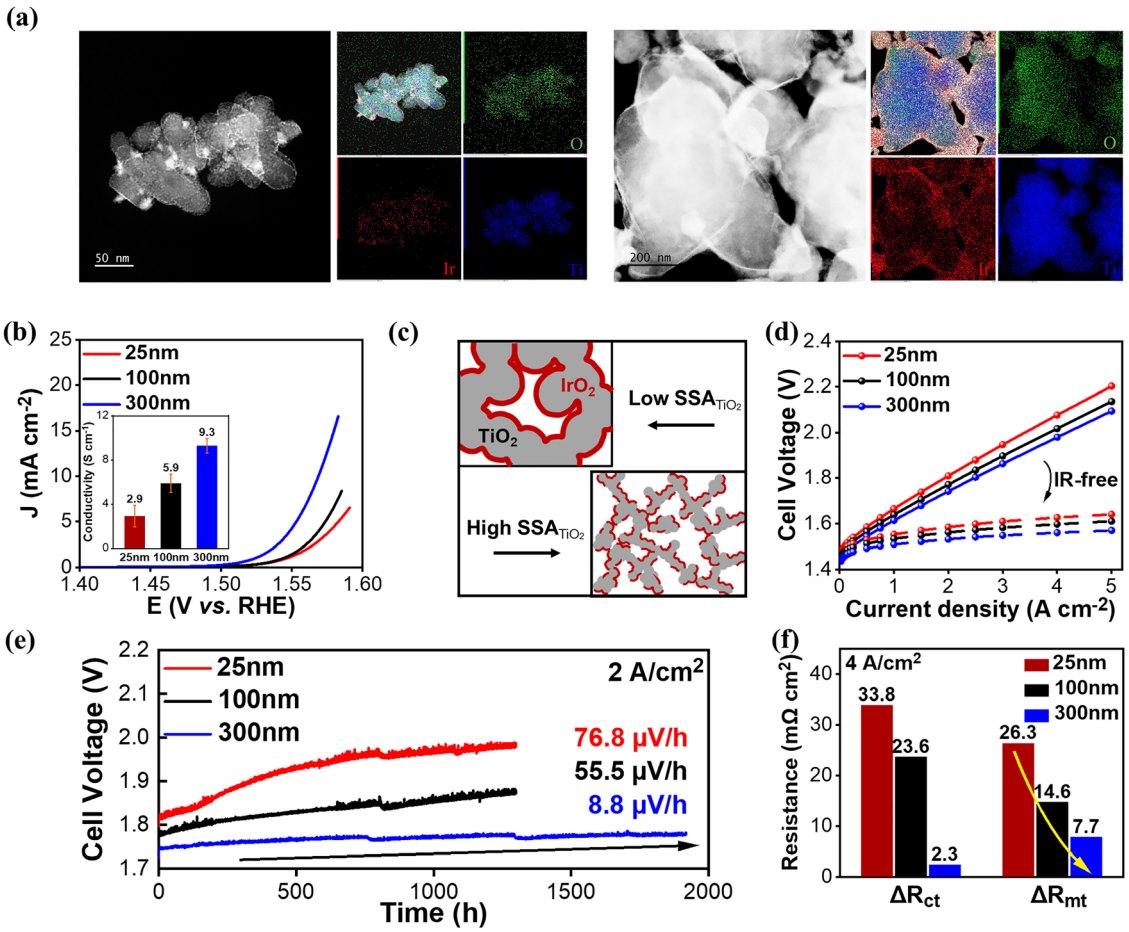

Fig. 5 Performance and stability of catalysts with 30% loading. (a) HAADF-STEM image and EDX elemental mappings of 25 nm and 300 nm catalysts. (b) Linear sweep voltammetry curves in the RDE. (c) Structural schematic diagram of the 25 nm and 300 nm catalysts with 30% loading. (d) Polarization curves in the PEMWE cell. (e) Durability test at 2.0 A cm^{-2} and 80 °C. (f) Fitted R_{ct} and R_{mt} variations of all ACLs after 1300-hour durability.

(Fig. S13) showed that the contributions of η_{ct}, η_{ohm}, and η_{mt} to the overall performance difference were approximately 33.9%, 31.2%, and 34.9%, respectively, indicating that no single process could fully account for the overall performance gap.

The 300 nm ACL retained a richer pore structure, enabling rapid oxygen release within the ACL (Fig. S14 and S15). These kinetic differences collectively explained the performance discrepancies, resulting in differences in the overall catalyst utilization. Calculated following the methods of Padgett *et al.*,[40] the catalyst utilization of the 300 nm–30% ACL was 26.3% at 2 A cm^{-2}, compared to only 10.2% for the 25 nm–30% ACL, as shown in Fig. S16 and Table S1.

In the PEMWE stability test at 80 °C and 2 A cm^{-2}, the 300 nm–30% ACL exhibited remarkable stability, attributed to its superior intrinsic activity and efficient mass transport channels. Over 1900 hours of operation, its voltage decay rate was just 8.8 μV h^{-1}, nearly nine times lower than the 76.8 μV h^{-1} decay rate of the 25 nm–30% ACL (Fig. 5e). After 1300 hours of testing, this discrepancy led to a voltage difference of 212 mV. The polarization curve after stability testing revealed even greater voltage differences at high current densities, with the voltage difference reaching 269 mV at 4 A cm^{-2} (Fig. S17a). Further loss separation analysis indicated that the discrepancy primarily arose from variations in η_{mt} and η_{ohm}. At 4 A cm^{-2}, the 25 nm–30% ACL displayed a larger mass transport arc after stability testing, with R_{mt} increasing rapidly by 26.3 mΩ cm^2. The hindered removal of gaseous products accelerated long-term degradation. After aging, pronounced penetrating cracks were observed in the 25 nm–30% ACL (Fig. S18), indicative of irreversible structural damage driven by localized stresses arising from gas entrapment. In contrast, the 300 nm–30% ACL maintained its structural integrity after aging.

The limited mass transport channels in the 25 nm–30% ACL further constrained the expression of active sites due to physical disintegration of the ACL, leading to a greater increase in R_{ct} compared to the 300 nm–30% ACL. In contrast, the 300 nm–30% ACL showed no mass transport issues after 800 hours and exhibited only a slight increase of 7.7 mΩ cm^2 in R_{mt} after 1300 hours (Fig. 5f and Fig. S19a and b). Variations in η_{ohm} were primarily driven by HFR. This difference stemmed from restricted mass transport channels, which facilitated gas bubble accumulation on the ACL surface, thereby exacerbating contact resistance and significantly increasing HFR.[41] The HFR difference between the 25 nm–30% ACL and 300 nm–30 ACL increased by 272%, rising from 7.7 mΩ cm^2 to 28.4 mΩ cm^2, compared with the pre-stability period (Fig. S19c).

In summary, the ACL prepared with large-particle-size catalysts at reduced loading not only retained its original, rich pore structure but also exhibited enhanced catalyst intrinsic activity, attributed to differences in electrical conductivity. These advantages collectively contributed to the superior performance and stability of the 300 nm–30% ACL in PEMWE.

Conclusion

In conclusion, our study highlights the critical role of the support's specific surface area in determining the performance and durability of ACLs under operational conditions. Paradoxically, large-particle supports with a lower specific surface area, often overlooked in conventional approaches, instead exhibit superior performance and exponentially enhance stability in PEMWE systems. This is due to the dual optimization of both the catalyst and electrode structure. It not only involves forming continuous precious metal shells to improve catalyst conductivity, but it also optimizes the porosity structure of ACLs through the rapid stacking of low bulk density ink, synergistically enhancing the precious metal utilization.

Experiment section

Materials

$HIrCl_6{\cdot}xH_2O$ (35.7 wt%, Sino-Platinum Metal Co., Ltd); Nafion 115 membrane (127 μm, DuPont Company, USA); Nafion solution (D2020 from DuPont Company, USA); Aquivion ionomers (D31579 from Solvay S.A., Belgium); 2-propanol (purity ≥ 99.9%, from Sigma-Aldrich), *n*-propanol (NPA, purity ≥ 99.9%, from Sigma-Aldrich), 1,2-propanediol (1,2-PG, purity ≥99.9%, from Sigma-Aldrich), ethanol (EtOH, purity ≥99.9%, from Sigma-Aldrich) and de-ionized (DI) water (18 MΩ cm); ZrO_2 grinding balls (2 mm); 60% wt Pt/C (Johnson Matthey Company, UK).

Synthesis of prototype oxygen evolution reaction catalysts

Specifically, 1.22 g of $H_2IrCl_6{\cdot}xH_2O$ was dissolved in 10 mL of isopropanol and ultrasonicated for 10 minutes. The precursor solution was dropwise added to the 300 nm-TiO_2 suspension (500 mg 300 nm TiO_2 dispersed in 50 mL of H_2O) by stirring. The mixture was then dried in an oven for 60 min at 80 °C and mixed with finely ground $NaNO_3$. After that, the mixed powder was further ground, followed by a calcination process at 450 °C for 1 h. The obtained metal oxide was naturally cooled and washed with DI water to remove the salts. The final product was obtained as dark blue powder after drying in air at 80 °C overnight. Supported IrO_2 on 25 nm and 100 nm TiO_2 was prepared as described above except that the support was replaced with different particle size TiO_2.

Electrochemical characterization in the three-electrode system

Typically, 2.1 mg of the catalysts were dispersed in the mixture of 295 μL of isopropanol, 700 μL of water, and 5 μL of 5 wt% Nafion solution. At the temperature lower than 25 °C, the suspension was ultrasonicated for 30 minutes until well-dispersed catalyst ink was formed. Then, 10 μL of the catalyst ink was drop-casted on a glassy carbon disk electrode (diameter 5 mm, Pine Research Instrumentation), which was used as the working electrode.

All linear sweep voltammetry (LSV) studies were carried out in the 0.5 M H_2SO_4 supporting electrolyte using a CHI 760E potentiostat in a three-electrode configuration. The catalyst-loaded glassy carbon disk electrode was applied as the working electrode. The home-designed reversible hydrogen electrode (RHE) was used as the reference electrode (a platinum sheet electrode with hydrogen gas bubbling near the electrode).

A platinum sheet (1 cm × 1 cm) was used as the counter electrode. The working electrode was then rotated at 1600 rpm which was controlled by a Pine MSR rotator system. At 25 °C, LSV scans were recorded at a rate of 5 mV s^{-1} from 1.3 V to 1.6 V *vs.* RHE. Each LSV was recorded 3 times to ensure repeatability.

Cyclic voltammetry (CV) was conducted to evaluate the electrochemical surface area of the three catalysts. The applied voltage ranged from 0.3 V to 1.5 V at a fixed rate of 50 mV s^{-1}.

Catalyst coated membrane (CCM) preparation

Catalyst ink was made from the three catalyst powder, Aquivion ionomers (D31579), and dispersion solvents. When the catalyst loading is 50%, the anode electrode was fabricated by the ink, which was DI water, NPA and 1,2-PG mixed solution with a mass ratio of 6 : 2 : 2. The solid content of the ink was 27.5 wt% and the mass of the ionomers was 10 wt% of the catalyst. When the catalyst loading is 30%, the anode electrode was fabricated by the ink, which was DI water, NPA, 1,2-PG and EtOH mixed solution with a mass ratio of 3 : 1 : 1 : 1.The solid content of the ink was 30 wt% and the mass of the ionomers was 10 wt% of the catalyst. All inks were prepared by ball milling at a speed of 300 rpm for 4 hours. For the cathode electrodes, 60% wt Pt/C was used as the catalyst. Catalyst inks were prepared from catalyst powder, Nafion solution (D2020), 2-propanol, and DI water. The inks were dispersed through ball milling at a speed of 300 rpm for 4 hours. Both anode and cathode catalyst inks were coated on the PTFE cell (thickness of 50 μm) by a blade coating machine after ball milling. After infrared light drying at 120 °C for 4 minutes, both electrodes were hot-pressed on a Nafion 115 membrane by a decal transfer process at 140 °C and 2 MPa for 3 minutes. The catalyst loadings of both sides were determined by using an X-ray fluorescence (XRF) spectrometer. The Pt loading on cathode electrodes is 0.3 ± 0.03 mg cm^{-2} with an I/C ratio of 0.625. The Ir loading on anode electrodes is 0.5 ± 0.05 mg cm^{-2}.

Characterization of the catalysts and the ACLs

The energy-dispersive X-ray (EDX) spectrometry elemental mapping and the HAADF-STEM images were recorded for the three catalysts based on a transmission electron microscope equipped with a probe corrector (JEOL-ARM300F2, Japan) operating at 300 kV. SEM studies were performed on a field emission scanning electron microscope (FE-SEM, Zeiss GeminiSEM 500, Germany). Specific surface area and pore analyses were performed using a physical adsorption instrument (TriStar II 3020, USA) and a mercury porosimeter (AutoPore lV 9500, USA).

Electrochemical characterization in PEMWE

The electrolyzer tests were performed on a four-channel electrolyzer test station (LQ-4C-100, Amoy Island Hydrogen (Xiamen) Technology Co., Ltd). The PEMWE cell with an active area of 4.0 cm^2 was operated at the temperature of 80 °C with the ultra-pure water (18.2 MΩ cm) feeding only through the anode at a flow rate of 100 mL min^{-1}. The membrane electrode assembly (MEA) was constructed by placing the CCM between the porous transport layers (PTLs), for which platinum-coated titanium felts (56% porosity with a thickness of 250 μm, Bekaert Company, Belgium) and carbon papers (TGP-H-060 from Toray Company, Japan) were used for anode and cathode PTL, respectively. After warming up, PEMWE was conditioned by ramping the current to 2 A cm^{-2} and holding it for 4 hours. Then, the performance of PEMWE was evaluated by measuring the polarization curve through staircase linear sweep AC voltammetry (Solartron EnergyLab impedance analyzer (20 A), England). The voltage scan was set from 1.3 V to 2.1 V at a rate of 1 mV s^{-1} with a step of 10 mV. To obtain the high-frequency resistance (HFR), EIS was conducted in each voltage step with the frequency ranging from 10 kHz to 100 Hz and amplitude at 10 mV. The HFR was acquired from the high-frequency intercept of the Nyquist plot with the real axis. Each polarization curve was repeated 3 times to get repeatable values. Galvanostatic electrochemical impedance spectroscopy (GEIS) was performed after recording the polarization curve with the frequency ranging from 10 kHz to 0.1 Hz. The amplitude of the current perturbation was chosen for each step to obtain a sufficient signal to noise ratio, while keeping the perturbation small enough to ensure a linear system response. The transmission-line model was applied to fit the results.

Breakdown of distinct kinetic processes was performed to better understand each process. The overall cell voltage can be defined by the following equation:

$$E_{cell} = E_{rev} + \eta_{ohm} + \eta_{ct} + \eta_{mt} \quad (1)$$

where E_{rev} is the reversible cell voltage, which is approximately 1.18 V at 80 °C, η_{ohm} is the ohmic overpotential of the proton and electron transport resistance, η_{ct} is the activation overpotential of electrocatalysis, which is dominated by the anodic oxygen evolution reaction, and η_{mt} is the mass transport overpotential induced by water and gas flow. The value of η_{ohm} is calculated by R_{ohm} fitted by high-frequency resistance from the EIS curve. The η_{ct} is fitted by the Tafel equation. As a result, three types of typical overpotentials can be separated.

Cyclic voltammetry (CV) was conducted to evaluate the electrochemical surface area of ACLs. The applied voltage ranged from 0.3 V to 1.2 V at a fixed rate of 50 mV s^{-1}. During the measurement, the cathode side was purged with H_2 to simulate the RHE.

Multiple dynamic light scattering (MDLS)

MDLS technology (TURBISCAN TOWER, France) was used to evaluate the stability of dispersion, including the migration of particles and variation of particle size, *etc.*[15] Incident photons undergo multiple scattering events before absorption, with the transmission of neglectable photons through the sample in our cases. The final scattering light depends on the wavelength of the incident light, the concentration and size of solid particles, and the refractive index of solvents and solutes. Herein, the wavelength of incident light is around 880 nm, thus the change of backscattering (BS) intensity over time only depends on the variation of particle concentration and size in the dispersions. When the particle size is smaller than the wavelength of the

incident light, BS intensity increases with increasing particle size. When the particle size is larger than the wavelength, BS intensity decreases with increasing article size. According to the TURBISCAN TOWER production information, the critical average diameter is around 600 nm. In the multiple scattering regimes, the BS intensity increases with particle volume fraction for randomly distributed scatters. However, for highly concentrated suspensions, dependent scattering effects induce an increase in the transport path length and a consequent fall in the diffuse reflectance BS, causing the BS intensity to decrease with particle volume fraction increasing. Delta backscattering intensity (delta BS), defined as the difference between BS and initial BS divided by initial BS, was used to evaluate the system stability in this paper, as shown in eqn (2).

$$\Delta BS = \frac{BS(t) - BS(t_0)}{BS(t_0)} \quad (2)$$

During the measurement, catalyst ink was placed in a 5 mL transparent glass bottle, and the probe scanned from bottom to top of the bottle to detect the change of particle size and concentration by BS.

Rheology measurement protocol

Rheological measurements were carried out using a stress-controlled rheometer (DHR-20, TA Instruments, USA). Measurements were performed at 25 °C using a stainless-steel conical plate geometry (60 mm diameter) with a gap of 29 μm. Stable shear rheology measurements were performed by applying shear rate scans in logarithmic decrements from 0.5 to 100 s^{-1}.

Conflicts of interest

There are no conflicts to declare.

Data availability

The data supporting this article have been included as part of the SI. The supplementary information includes detailed experimental data, additional figures, and tables that support the findings of this study. See DOI: **https://doi.org/10.1039/d5mh01127b**

Acknowledgements

This work was supported by the National Key R&D Program of China (2023YFB4004600 and 2024YFB4207300), the Major Science and Technology Project of Xiamen Municipal Government (3502Z20241030), the Science and Technology Projects (RD2021010401) of the Innovation Laboratory for Sciences and Technologies of Energy Materials of Fujian Province (IKKEM), the Science and Technology Project (2022L3077) of Fujian Province, and the New Cornerstone Science Foundation.

References

1 C. Minke, M. Suermann, B. Bensmann and R. Hanke-Rauschenbach, *Int. J. Hydrogen Energy*, 2021, **46**, 23581–23590.
2 C. Wang, A. Schechter and L. Feng, *Nano Res. Energy*, 2023, **2**, e9120056–e9120056.
3 L. Moriau, M. Bele, Ž. Marinko, F. Ruiz-Zepeda, G. Koderman Podboršek, M. Šala, A. K. Šurca, J. Kovač, I. Arčon, P. Jovanovič, N. Hodnik and L. Suhadolnik, *ACS Catal.*, 2021, **11**, 670–681.
4 H. N. Nong, H. Oh, T. Reier, E. Willinger, M. Willinger, V. Petkov, D. Teschner and P. Strasser, *Angew. Chem., Int. Ed.*, 2015, **54**, 2975–2979.
5 G. Liu, J. Xu, Y. Wang and X. Wang, *J. Mater. Chem. A*, 2015, **3**, 20791–20800.
6 W. Hu, S. Chen and Q. Xia, *Int. J. Hydrogen Energy*, 2014, **39**, 6967–6976.
7 H. Oh, H. N. Nong and P. Strasser, *Adv. Funct. Mater.*, 2015, **25**, 1074–1081.
8 L. Xu, Q. Jiang, Z. Xiao, X. Li, J. Huo, S. Wang and L. Dai, *Angew. Chem., Int. Ed.*, 2016, **128**, 5363–5367.
9 H.-S. Oh, H. N. Nong, T. Reier, M. Gliech and P. Strasser, *Chem. Sci.*, 2015, **6**, 3321–3328.
10 M. A. Mahmoud, C. E. Tabor, M. A. El-Sayed, Y. Ding and Z. L. Wang, *J. Am. Chem. Soc.*, 2008, **130**, 4590–4591.
11 T. Lazaridis, B. M. Stühmeier, H. A. Gasteiger and H. A. El-Sayed, *Nat. Catal.*, 2022, **5**, 363–373.
12 D. Hoffmeister, S. Finger, R. Pokhrel, A. Körner, B. Fritsch, S. Thiele, A. Hutzler and C. Pham, *Chem. Eng. J.*, 2025, **517**, 164281.
13 M. Bernt, C. Schramm, J. Schröter, C. Gebauer, J. Byrknes, C. Eickes and H. A. Gasteiger, *J. Electrochem. Soc.*, 2021, **168**, 084513.
14 M. Bernt, A. Siebel and H. A. Gasteiger, *J. Electrochem. Soc.*, 2018, **165**, F305.
15 Q. Wang, Y. Cheng, H. B. Tao, Y. Liu, X. Ma, D. Li, H. B. Yang and B. Liu, *Angew. Chem., Int. Ed.*, 2023, **135**, e202216645.
16 M. Li, P. Xie, L. Yu, L. Luo and X. Sun, *ACS Nano*, 2023, **17**, 23299–23316.
17 Y. J. Kim, A. Lim, J. M. Kim, D. Lim, K. H. Chae, E. N. Cho, H. J. Han, K. U. Jeon, M. Kim, G. H. Lee, G. R. Lee, H. S. Ahn, H. S. Park, H. Kim, J. Y. Kim and Y. S. Jung, *Nat. Commun.*, 2020, **11**, 4921.
18 T. A. M. Suter, K. Smith, J. Hack, L. Rasha, Z. Rana, G. M. A. Angel, P. R. Shearing, T. S. Miller and D. J. L. Brett, *Adv. Energy Mater.*, 2021, **11**, 2101025.
19 C. V. Pham, M. Bühler, J. Knöppel, M. Bierling, D. Seeberger, D. Escalera-López, K. J. J. Mayrhofer, S. Cherevko and S. Thiele, *Appl. Catal., B*, 2020, **269**, 118762.
20 C. Felix, B. J. Bladergroen, V. Linkov, B. G. Pollet and S. Pasupathi, *Catalysts*, 2019, **9**, 318.
21 J. Islam, B. S. Yoon, P. T. Thien, C. H. Ko and S.-K. Kim, *Catal. Today*, 2024, **425**, 114349.
22 E. Oakton, D. Lebedev, M. Povia, D. F. Abbott, E. Fabbri, A. Fedorov, M. Nachtegaal, C. Copéret and T. J. Schmidt, *ACS Catal.*, 2017, **7**, 2346–2352.

23 B. Jiang, Y. Guo, J. Kim, A. E. Whitten, K. Wood, K. Kani, A. E. Rowan, J. Henzie and Y. Yamauchi, *J. Am. Chem. Soc.*, 2018, **140**, 12434–12441.
24 C. Wei, S. Sun, D. Mandler, X. Wang, S. Zhang Qiao and Z. J. Xu, *Chem. Soc. Rev.*, 2019, **48**, 2518–2534.
25 H. Liu, H. B. Tao and B. Liu, *J. Phys. Chem. Lett.*, 2022, **13**, 6520–6531.
26 S. Wang, J. Zhang, O. Gharbi, V. Vivier, M. Gao and M. E. Orazem, *Nat. Rev. Methods Primers*, 2021, **1**, 1–21.
27 J. He, B. Hu and Y. Zhao, *Adv. Funct. Mater.*, 2016, **26**, 5998–6004.
28 H. Chen, X. Liang, Y. Liu, X. Ai, T. Asefa and X. Zou, *Adv. Mater.*, 2020, **32**, 2002435.
29 H. Lv, S. Wang, Y. Sun, J. Chen, W. Zhou and C. Zhang, *J. Power Sources*, 2023, **564**, 232878.
30 C. Tang, H.-F. Wang and Q. Zhang, *Acc. Chem. Res.*, 2018, **51**, 881–889.
31 C. Spöri, J. T. H. Kwan, A. Bonakdarpour, D. P. Wilkinson and P. Strasser, *Angew. Chem., Int. Ed.*, 2017, **56**, 5994–6021.
32 B. Tjaden, D. J. L. Brett and P. R. Shearing, *Int. Mater. Rev.*, 2018, **63**, 47–67.
33 Y. J. Kim, A. Lim, J. M. Kim, D. Lim, K. H. Chae, E. N. Cho, H. J. Han, K. U. Jeon, M. Kim, G. H. Lee, G. R. Lee, H. S. Ahn, H. S. Park, H. Kim, J. Y. Kim and Y. S. Jung, *Nat. Commun.*, 2020, **11**, 4921.
34 S. Prass, J. St-Pierre, M. Klingele, K. A. Friedrich and N. Zamel, *Electrocatalysis*, 2021, **12**, 45–55.
35 N. Azema, *Powder Technol.*, 2006, **165**, 133–139.
36 C. Tisserand, G. Brambilla, G. Meunier and A. Parker, *J. Dispersion Sci. Technol.*, 2020, **41**, 648–655.
37 S. Chen, Y. Liu, X. Fu and W. Wang, *Front. Energy*, 2024, **18**, 330–355.
38 S. Khandavalli, J. H. Park, N. N. Kariuki, S. F. Zaccarine, S. Pylypenko, D. J. Myers, M. Ulsh and S. A. Mauger, *ACS Appl. Mater. Interfaces*, 2019, **11**, 45068–45079.
39 P. Mazúr, J. Polonský, M. Paidar and K. Bouzek, *Int. J. Hydrogen Energy*, 2012, **37**, 12081–12088.
40 E. Padgett, G. Bender, A. Haug, K. Lewinski, F. Sun, H. Yu, D. A. Cullen, A. J. Steinbach and S. M. Alia, *J. Electrochem. Soc.*, 2023, **170**, 084512.
41 T. Schuler, T. J. Schmidt and F. N. Büchi, *J. Electrochem. Soc.*, 2019, **166**, F555.

